

Giant Anomalous Hall and Nernst Conductivities in Magnetic All-*d* Metal Heusler Alloys

Mohammad Farhan Tanzim, Nuno Fortunato, Ilias Samathrakakis, Ruiwen Xie,*
Ingo Opahle, Oliver Gutfleisch, and Hongbin Zhang

All-*d* Heuslers are a category of novel compounds combining versatile functionalities such as caloric responses and spintronics with enhanced mechanical properties. Despite the promising transport properties (anomalous Hall (AHC) and anomalous Nernst (ANC) conductivities) shown in the conventional Co_2XY Heuslers with *p-d* hybridization, the all-*d* Heuslers with only *d-d* hybridization open a new horizon to search for new candidates with outstanding transport properties. In this work, the AHC and ANC are evaluated for thermodynamically stable ferro/ferri-magnetic all-*d*-metal regular Heusler compounds based on high-throughput first-principles calculations. It is observed that quite a few materials exhibit giant AHCs and ANCs, such as cubic Re_2TaMn with an AHC of 2011 S cm^{-1} , and tetragonal Pt_2CrRh with an AHC of 1966 S cm^{-1} and an ANC of $7.50 \text{ A m}^{-1}\text{K}^{-1}$. Comprehensive analysis on the electronic structure reveals that the high AHC can be attributed to the occurrence of the Weyl nodes or gapped nodal lines in the neighborhood of the Fermi level. The correlations between such transport properties and the number of valence electrons are also thoroughly investigated, which provides a practical guidance to tailor AHC and ANC via chemical doping for transverse thermoelectric applications.

particular, for magnetic materials with broken time-reversal symmetry, anomalous Hall conductivity (AHC) and anomalous Nernst conductivity (ANC) are the most representative linear response transport properties of the topological origin,^[7,8] making such materials applicable as field sensors, memory devices, thermoelectric power generators and heat-flux sensors.^[9–11] AHC describes the generation of a transverse voltage by an applied longitudinal current, whereas finite ANC emerges under a temperature gradient instead of a current.^[10] For instance, sufficiently large ANC can be applied to design transverse thermoelectric devices,^[12] thus it is interesting to screen for more candidates exhibiting large AHC and ANC.

Heusler compounds are a class of materials hosting multifunctional properties driven by their versatile compositions for tunable physical properties.^[13] They serve as an ideal playground for spintronics because of their high spin polarization


1. Introduction

In the last two decades, topological phenomena driven by the nontrivial geometric phase^[1] and topological materials have attracted significant attention; they are especially promising for sophisticated electronic and spintronic applications.^[2–6] In

and low magnetic damping coefficient.^[14] In terms of topological properties, there are many ternary half-Heusler compounds which can be classified as topological insulators.^[15] Moreover, as demonstrated by Manna *et al.*, independent of the magnetization, AHC in the magnetic Heusler compounds can be controlled via the interplay of the crystal symmetry with the topological and geometrical properties of the Berry curvature (BC).^[16] Recently, magnetic materials with vanishing band gaps but nontrivial topological properties are becoming interesting, such as spin gapless semiconductors^[17,18] and Weyl semimetals.^[19] It has been reported that the ferromagnetic (FM) Co_2MnGa possesses a giant ANC,^[20,21] as well as a strong AHC response.^[22] Based on the angle-resolved photoemission spectroscopy (ARPES) and the *ab-initio* calculations, Belopolski *et al.*^[22] suggested the potent contribution from topological nodal lines to the large ANC of Co_2MnGa . However, for Co-based Heuslers, the Seebeck coefficient corresponding to the anomalous Nernst effect (ANE), being $6\text{--}8 \mu\text{V K}^{-1}$,^[23,24] is still several orders of magnitude smaller than those of nowadays thermoelectric materials. Another route to achieve well-performed transverse thermoelectric properties is via engineering the contributions of the Seebeck effect (SE) and the anomalous Hall effect (AHE). For instance, the $\text{Co}_2\text{MnGa/Si}$ hybrid material hosts a SE-driven transverse thermopower several orders

M. F. Tanzim, N. Fortunato, I. Samathrakakis, R. Xie, I. Opahle, H. Zhang
Theory of Magnetic Materials
Institute of Materials Science
Technical University of Darmstadt
64287 Darmstadt, Germany
E-mail: ruiwen.xie@tmm.tu-darmstadt.de

O. Gutfleisch
Functional Materials
Institute of Materials Science
Technical University of Darmstadt
64287 Darmstadt, Germany

 The ORCID identification number(s) for the author(s) of this article can be found under <https://doi.org/10.1002/adfm.202214967>.

© 2023 The Authors. Advanced Functional Materials published by Wiley-VCH GmbH. This is an open access article under the terms of the Creative Commons Attribution-NonCommercial License, which permits use, distribution and reproduction in any medium, provided the original work is properly cited and is not used for commercial purposes.

DOI: 10.1002/adfm.202214967

of magnitude higher than the ANE-driven thermopower.^[25] In principle, the SE of the thermoelectric material Si generates a longitudinal electric field E under an applied temperature gradient ΔT , which in turn induces a charge current in the magnetic material Co_2MnGa that is then converted into transverse E by the AHE.

To search for more Heusler compounds with enhanced topological transport properties, high-throughput (HTP) density functional theory (DFT) calculations are essential, where the intrinsic topological properties can be straightforwardly evaluated by constructing accurate tight-binding representation of the electronic structure based on Wannier functions.^[26,27] Noky *et al.*^[28] have performed calculations on the intrinsic topological transport properties of the magnetic cubic full Heusler compounds and identified several new Heusler compounds with enhanced AHC and ANC.^[29] In addition, by collecting the experimentally available full and inverse Heusler compounds and evaluating both the spin Hall conductivity (SHC) and AHC, Ji *et al.*^[29] have suggested such compounds as promising candidates for spintronic applications. Going beyond the conventional Heusler compounds X_2YZ , which are stabilized by the p - d covalent bonding between the X and Z atoms, Wei *et al.* synthesized the first Heusler phase Ni_2MnTi consisting of only d elements.^[30] Such all- d -metal Heuslers are expected to have very useful mechanical properties due to the d - d bonding and have been largely studied in terms of magnetocaloric properties.^[31–35] Moreover, many compositions have been predicted to show robust magnetic properties, for example, high Curie temperature, tunable hysteresis properties in useful temperature ranges and capability of maintaining magnetic order upon chemical disorder,^[35,36] which makes them functional as spintronics. Note that there has been an HTP screening performed to screen for Co-based all- d -metal Heuslers, focusing on the thermodynamic stability and the elementary magnetic properties.^[37] However, proper characterization of their topological properties is still missing.

In this work, we conduct HTP calculations to evaluate the AHC and ANC for a total number of 344 ferro/ferri-magnetic all- d -metal cubic and tetragonal regular Heusler compounds. Compounds with enhanced AHC and ANC are predicted. Moreover, detailed analyses on two typical systems, cubic Re_2TaMn and tetragonal Ni_2VMn , reveal that the mechanisms for the noticeable AHC can be attributed to the occurrence of Weyl nodes and the spin-orbit coupling (SOC) induced small band gaps close to the Fermi energy, respectively.

2. Results and Discussion

The magnetic ground states of the selected 344 all- d Heuslers are confirmed to be FM or ferrimagnetic through our DFT calculations,^[38] thus for the calculations of AHC and ANC, we set the magnetization direction along the [001] axis for both cubic and tetragonal structures.

Among the 344 compounds, 146 of them have cubic structure (Space Group 225) and 198 of them have tetragonal structure (Space Group 139). It is worth noting that a few all- d Heuslers have already been successfully synthesized in literature. For instance, Co_2MnTi and Mn_2PtPd were prepared by arc melting

and their magnetic properties were characterized.^[37] The optimized lattice structure of Co_2MnTi in our work is cubic with lattice parameter of 5.84 Å (see Table S1, Supporting Information), which is in close agreement with the experimental lattice parameter of 5.89 Å. For Mn_2PtPd , it was verified both experimentally and theoretically to be antiferromagnetic (AFM) and tetragonally distorted. However, our HTP screening focuses on FM and ferrimagnetic ground states in which a finite AHC/ANC is allowed with broken time reversal symmetry and broken invariance under spin rotation due to SOC. Thus, the compounds with collinear AFM structure as in Mn_2PtPd are excluded due to the presence of time reversal symmetry.^[39] Recently, Co_2MnV was synthesized using the arc-melting method and was found to be a cubic Heusler but with multiphases.^[40] Based on the calculated Bain path (see Figure S1, Supporting Information), a double-well feature at $c/a = 1$ and $c/a = 1.42$ can be observed. Although the Co_2MnV is predicted to be more stable under $c/a = 1.42$, the small energy difference between the cubic and tetragonal phases can be readily overcome by, for example, the temperature effect, which justifies its experimental characterization of being cubic. The DFT-based calculations are performed at zero Kelvin while in reality the synthesis conditions are usually under finite temperatures. Nevertheless, considering the high versatility of available synthesis techniques and processing parameters,^[41] the DFT-based predictions on the (meta-)stable phases in this work can be regarded as good references to guide future experimental studies.

The calculated z -components of the AHC ($\sigma_z = \sigma_{xy}$) and ANC ($\alpha_z = \alpha_{xy}$, at 300 K) for the cubic and tetragonal Heuslers are demonstrated in Figure 1a,b, respectively, in comparison with the values of AHC and ANC in the literature. For the Heuslers with superior transport properties, we list in Table 1 the magnitudes of their AHC and ANC. As listed in Table 1, there are 27 compounds (10 cubic + 17 tetragonal) which show AHC larger than $|1000| \text{ S cm}^{-1}$ and 14 compounds (2 cubic + 12 tetragonal) which exhibit ANC greater than $|5| \text{ A m}^{-1}\text{K}^{-1}$. In particular, three Pt-based tetragonal Heuslers, that is, Pt_2RhCr , Pt_2NiCo , and Pt_2RhCo , display simultaneously high AHC and ANC. Moreover, Re_2TaMn is predicted to possess a giant AHC of approximately 2011 S cm^{-1} at the Fermi level, which is higher than the already experimentally realized 1600 S cm^{-1} for Co_2MnGa and $1800\text{--}2000 \text{ S cm}^{-1}$ for Co_2MnAl .^[42,43] Additionally, as the maxima of AHC and ANC can be tailored by shifting the Fermi energy level via doping,^[44] Table 1 includes also those compounds with significant maximal AHC and ANC (AHC_{max} and ANC_{max}) and the corresponding shifts with respect to the Fermi level. Taking Co_2NbMn and Fe_2NiCo as examples, their AHC_{max} are -1317 and 1636 S cm^{-1} , respectively, which are located at around 0.010 and -0.110 eV with respect to the Fermi level. From Table 1, we can also see that Os_2TaCr exhibits the highest magnitude of ANC of $-9.7 \text{ A m}^{-1}\text{K}^{-1}$, followed by Pt_2RhCo ($-9.5 \text{ A m}^{-1}\text{K}^{-1}$) and Os_2CrV ($-8.3 \text{ A m}^{-1}\text{K}^{-1}$). The magnitudes of ANC in these compounds are comparable to the highest ANC reported hitherto of $\text{Co}_3\text{Sn}_2\text{S}$ ($10 \text{ A m}^{-1}\text{K}^{-1}$ at 70 K).^[45] Again, despite the relatively low ANC of Co_2NbMn and Fe_2NiCo at the Fermi level, if doped they could be potential candidates for thermoelectric applications due to the reasonably high ANC_{max} close to the Fermi energy.^[25,46] The full list of the calculated AHC and ANC of the 344 all- d Heuslers is given in Table S1 (Supporting Information).

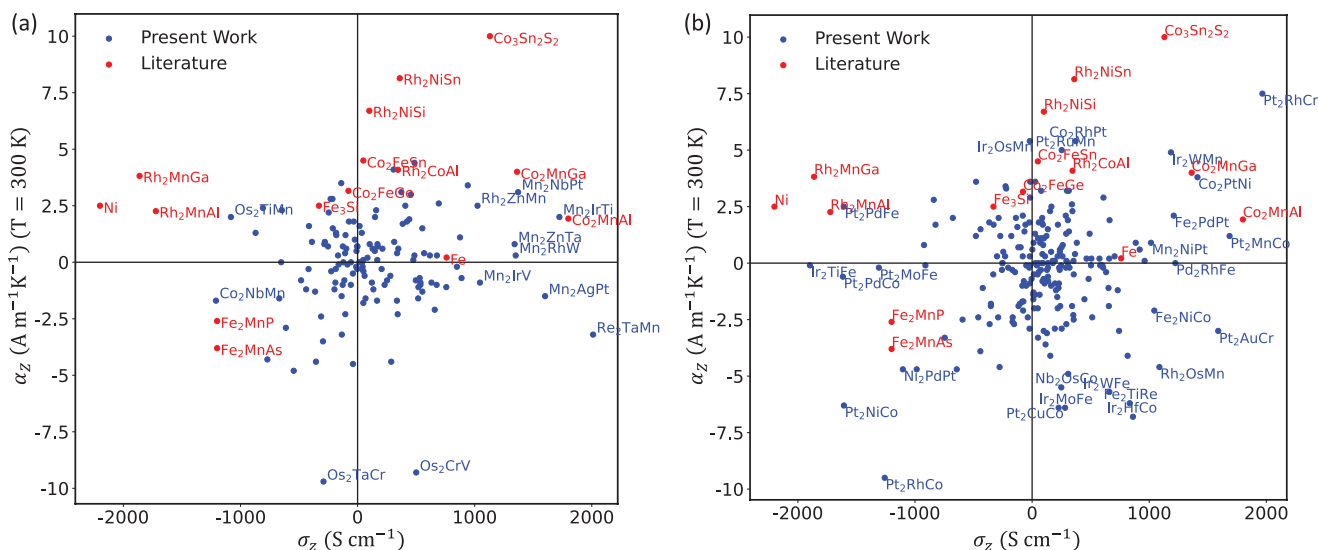


Figure 1. AHC and ANC (at 300 K) of selected materials with the magnetization direction parallel to the [001] direction for a) cubic and b) tetragonal all-*d* Heusler compounds. Results of present work are indicated with blue circles and the compositions are displayed for those with AHC larger than 1000 S cm⁻¹ or ANC larger than 5 A m⁻¹K⁻¹. For comparison, the materials and their AHC/ANC reported in the literature are marked by red circles.

To gain insights on the origin of the giant AHC and ANC, detailed analysis has been conducted on the electronic structure for two representative cases, that is, cubic Re₂TaMn and tetragonal Ni₂VMn. The crystal structure of Re₂TaMn is displayed in **Figure 2a** and the magnetization direction is along the [001] direction. The calculated AHC and ANC curves with respect to the Fermi energy are displayed in **Figure 2b,d**. An anomalous peak can be observed at the Fermi level for the AHC with the peak value being approximately 2011 S cm⁻¹. Regarding the ANC at 300 K, the maximum is located at 0.060 eV above the Fermi level and shows an absolute value as high as 8.2 A m⁻¹K⁻¹. Additionally, it can be noticed that the *x*- and *y*-components of AHC and ANC have vanishing magnitudes, suggesting that the AHC and ANC vector is parallel to the magnetization direction, as it can be interpreted based on symmetry.^[47]

Specifically, the shape of the AHC tensor depends on the direction of the magnetization. Since BC transforms as a pseudovector under the symmetry operations,^[48] the AHC and ANC tensors can be determined by finding the transformation of BC for all symmetries of the magnetic Laue group according to:

$$s\Omega(r) = \pm \det(D(R))D(R)\Omega(s^{-1}r), \quad (1)$$

where the BC pseudovector is represented by $\Omega(r)$, the 3D representation of a symmetry operation (excluding the translation symmetry) is given by $D(R)$, and an arbitrary symmetry operation is denoted by *s*. As a matter of fact, all the investigated Heusler compounds in the current work (both cubic and tetragonal) fall into the magnetic Laue group 4/*mm*'*m*' when the magnetization is applied along the [001] direction. In this case, the *m_z* mirror symmetry transforms the three components of the BC pseudovector in the following manner:

$$\begin{aligned} \Omega_x(k_x, k_y, -k_z) &= -\Omega_x(k_x, k_y, k_z), \\ \Omega_y(k_x, k_y, -k_z) &= -\Omega_y(k_x, k_y, k_z), \\ \Omega_z(k_x, k_y, -k_z) &= \Omega_z(k_x, k_y, k_z). \end{aligned} \quad (2)$$

Therefore, the summation of the BC over the entire Brillouin zone forces the AHC along the *x*- and *y*-axis to be zero, while leaving the component along the *z*-axis unrestricted, as the AHC itself depends on the BC according to Equation (3).

Furthermore, as Weyl points act as sources or sinks of BC^[1,49,50] which can lead to significant AHC and ANC when they are close to the Fermi energy,^[27,51] we search for Weyl points within ±50 meV around the Fermi energy. A total of 16 symmetry-related Weyl points are identified in Re₂TaMn, as illustrated in **Figure 2c** with the positive (negative) chiral charges marked by red (blue) arrows indicating the spatial direction of the Berry flux. The chirality of each Weyl point is calculated in terms of the shift of the Wannier charge centres^[50] and we list in **Table 2** the symmetry operations in the magnetic Laue group 4/*mm*'*m*', as well as their relations with the chirality. It can be first noticed that the sum of the chirality of the Weyl points within the Brillouin Zone (BZ) vanishes, as demonstrated in Nielsen–Ninomiya's theorem of Fermion doubling.^[52] Additionally, it can be explicitly seen from **Table 2** that the mirror planes, inversion symmetry and roto-inversions are responsible for the sign change of chirality. In **Figure 3a**, we plot out the band structure with SOC included along a specific *k* path which crosses a pair of Weyl nodes (-0.04, 0.30, 0.41) and (0.30, -0.04, 0.41). The presence of the Weyl points can be clearly observed, which are located at approximately 35 meV below the Fermi level. The calculated band structure without SOC effect is shown in **Figure 3a** for comparison. The Weyl point feature exists in the spin-up channel. The SOC effect, which mixes the spin-up and spin-down channels, slightly alters the *k* coordinates of the Weyl pair with respect to the spin-polarized case without SOC, and the energy position corresponding to the Weyl pair is closer to the Fermi level. The contribution of each Weyl point to the total AHC is subsequently evaluated by calculating the AHC within cubes of 0.17 unit length (in the reciprocal space) while keeping the Weyl points at the cubic centre. The total

Table 1. List of Heusler materials (X_2YZ) with promising transport properties, displaying theoretical lattice constants (a and c/a), Space Group (SG), AHC and ANC values (at Fermi-level), maximum AHC and ANC values within $\in [-0.250, 0.250]$ eV with respect to the Fermi-level (ΔE) and the total magnetic moment (M_{tot}) in unit of μ_B of the primitive cell.

Material	a Å	c/a	SG	AHC S cm ⁻¹	ANC A m ⁻¹ K ⁻¹	AHC _{max} [ΔE] S cm ⁻¹ [eV]	ANC _{max} [ΔE] A m ⁻¹ K ⁻¹ [eV]	M_{tot} μ_B
Co ₂ NbMn	5.96	1.00	225	-1210	-1.7	-1317 (0.010)	-5.6 (-0.050)	5.9
Co ₂ PtNi	5.14	1.45	139	1412	3.8	1646 (0.020)	-8.9 (0.250)	5.0
Co ₂ RhPt	5.37	1.36	139	371	5.4	-837 (-0.150)	-6.8 (-0.190)	4.9
Fe ₂ NiCo	5.13	1.34	139	1043	-2.1	1636 (-0.110)	6.4 (-0.190)	7.6
Fe ₂ PdPt	5.46	1.37	139	1209	2.1	1423 (0.110)	-4.8 (0.220)	6.8
Fe ₂ TiRe	5.95	1.00	225	834	-6.2	1606 (-0.190)	-7.6 (0.030)	2.8
Ir ₂ HfCo	5.60	1.38	139	861	-6.8	1636 (-0.040)	11.4 (-0.230)	1.7
Ir ₂ MoFe	5.47	1.39	139	282	-6.4	1867 (-0.080)	-7.1 (-0.020)	2.2
Ir ₂ OsMn	5.38	1.42	139	-20	5.4	-1067 (-0.100)	-6.9 (-0.250)	1.9
Ir ₂ TiFe	5.68	1.25	139	-1898	-0.1	-1931 (-0.010)	6.6 (0.120)	3.5
Ir ₂ WFe	5.48	1.38	139	660	-5.7	1341 (-0.170)	-5.8 (0.010)	2.3
Ir ₂ WMn	5.48	1.38	139	1185	4.9	2166 (0.250)	5.1 (0.020)	1.8
Mn ₂ AgPt	6.33	1.00	225	1601	-1.5	1846 (-0.100)	3.6 (-0.240)	8.2
Mn ₂ IrTi	6.03	1.00	225	1723	2.0	1979 (0.060)	11.0 (-0.190)	4.4
Mn ₂ IrV	5.99	1.00	225	1045	-0.9	1630 (-0.190)	5.8 (-0.250)	4.1
Mn ₂ NbPt	6.16	1.00	225	1371	3.1	1482 (0.040)	-4.7 (0.200)	5.1
Mn ₂ NiPt	5.77	1.16	139	1015	0.9	1587 (0.110)	2.4 (0.060)	8.4
Mn ₂ RhCo	6.04	1.00	225	1350	0.3	1354 (0.004)	-4.2 (0.210)	5.0
Mn ₂ ZnTa	6.02	1.00	225	1341	0.8	1481 (0.040)	5.4 (-0.120)	2.9
Nb ₂ OsCo	6.01	1.14	139	249	-5.5	1120 (-0.130)	-5.6 (0.010)	1.2
Ni ₂ PdPt	5.43	1.33	139	-1103	-4.7	-2675 (0.220)	-9.1 (-0.250)	2.2
Os ₂ CrV	6.03	1.00	225	501	-9.3	-1754 (0.150)	-11.4 (0.030)	2.6
Os ₂ TaCr	6.23	1.00	225	-291	-9.7	-1401 (0.100)	-9.7 (0.000)	2.8
Os ₂ TiMn	6.10	1.00	225	-1082	2.0	-1991 (-0.110)	-7.7 (-0.180)	3.0
Pd ₂ RhFe	5.42	1.45	139	1223	0.0	1354 (-0.010)	-6.7 (0.240)	5.1
Pt ₂ AuCr	5.64	1.40	139	1589	-3.1	2040 (-0.030)	5.4 (-0.190)	2.7
Pt ₂ CuCo	5.47	1.34	139	226	-6.4	1342 (-0.090)	-6.5 (0.010)	2.5
Pt ₂ MnCo	5.47	1.38	139	1686	1.2	1839 (0.030)	7.2 (-0.250)	5.9
Pt ₂ MoFe	5.42	1.47	139	-1308	-0.2	-1345 (0.010)	-3.4 (-0.060)	2.2
Pt ₂ NiCo	5.41	1.36	139	-1607	-6.3	-2158 (0.030)	-7.6 (0.030)	3.5
Pt ₂ PdCo	5.47	1.42	139	-1616	-0.6	-1715 (0.030)	-8.8 (-0.240)	3.0
Pt ₂ PdFe	5.53	1.41	139	-1608	2.5	-1694 (-0.180)	9.2 (0.080)	4.0
Pt ₂ RhCo	5.43	1.42	139	-1259	-9.5	-2154 (0.040)	-10.2 (-0.020)	3.1
Pt ₂ RhCr	5.46	1.43	139	1966	7.5	2432 (0.050)	10.1 (-0.050)	1.4
Pt ₂ RuMn	5.43	1.44	139	253	5.0	1154 (0.120)	-5.4 (0.150)	2.8
Re ₂ TaMn	6.23	1.00	225	2011	-3.2	2031 (0.003)	-8.2 (0.060)	2.3
Rh ₂ OsMn	5.35	1.43	139	1087	-4.6	2113 (-0.080)	-5.8 (0.160)	2.3
Rh ₂ ZnMn	6.03	1.00	225	1024	2.5	1959 (0.230)	-5.1 (0.250)	3.2

contributions of all the 16 Weyl points, whose total volume amounts to about 78% of the whole BZ, are then obtained by summing up the AHC resulting from the 16 cubes, which constitutes approximately 74% of the total AHC at the Fermi level (see Figure 3b).

In contrast to Re₂TaMn, we find that the singular behavior of the AHC and ANC in Ni₂VMn can be attributed to a different origin. Ni₂VMn is a regular tetragonal Heusler compound with $c/a = 1.48$ and total spin moment $\mu_S = 4.16 \mu_B$, in which Ni, Mn, and V have magnetic moments of 0.31, 2.40,

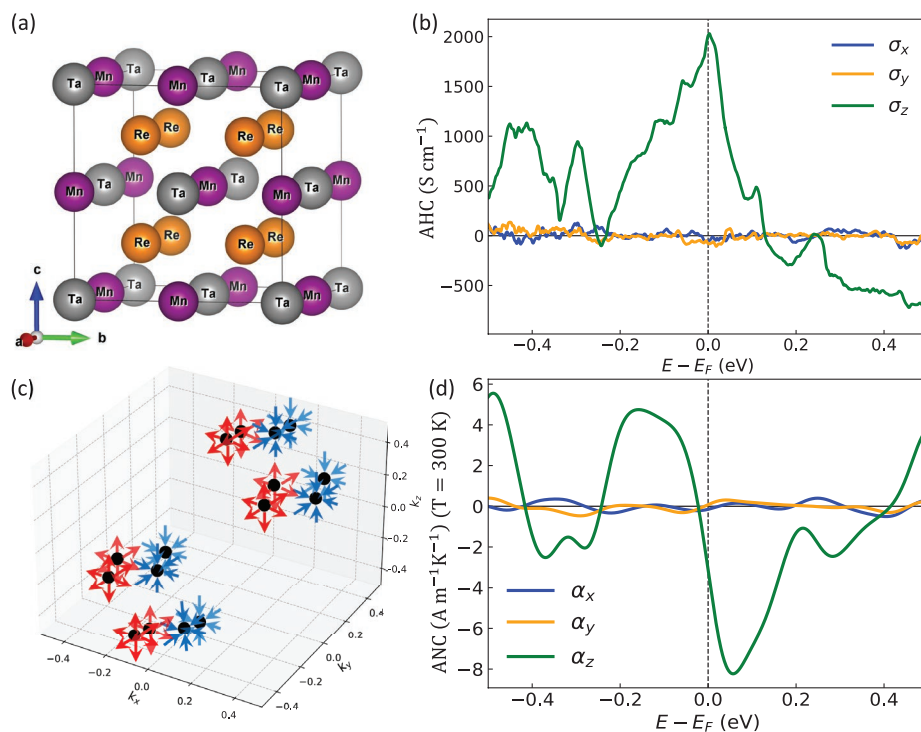


Figure 2. a) Crystal structure of Re_2TaMn (conventional cell). b) The components of the calculated AHC, σ_x , σ_y , and σ_z of Re_2TaMn , for the magnetization direction along the [001] direction. c) Illustration of the 16 identified Weyl points (in the k space with the unit of $2\pi/a$) in the Brillouin zone with Berry flux direction (The calculation is adopted in the primitive cell). Red and blue arrows around the Weyl point denote positive (source) and negative (sink) topological charges, respectively. d) The components of the calculated ANC at 300 K of Re_2TaMn , α_x , α_y , and α_z , for the magnetization direction along the [001] direction.

and $-0.92 \mu_B$, respectively. The AHC and ANC of Ni_2VMn are shown in Figure 4a,b. The absolute values of AHC and ANC at the Fermi level are 594.0 S cm^{-1} and $2.5 \text{ A m}^{-1}\text{K}^{-1}$, respectively. In order to identify the main contributor to the AHC, we divide the k space corresponding to the primitive cell of Ni_2VMn within $k_i \in [-0.5, 0.5]$ ($i = x, y, z$) into $6 \times 6 \times 6$ cubes and calculate the AHC within each cube (see the color map displayed in Figure 5a). The sum of the AHC values obtained in the 216 cubes is around -552.5 S cm^{-1} , which is close but slightly different from the calculated AHC by integrating the whole BZ owing to the different k -mesh density. Additionally, by investigating the band structure in the BZ having small band gaps, we notice that the locations of small band gaps are correlated with the blue regions as shown in Figure 5a. Taking the plane with $k_z = -0.16$ as an example (with reference to the middle left panel of Figure 5a), the shaded areas in Figure 5c are with band gaps smaller than 27 meV between two neighboring bands in the vicinity of the Fermi level. It can be found that for the region with $k_x \in (-0.17, 0.17)$ and $k_y \in (0.33, 0.50)$, the relatively large component of σ_z (dark blue area) is manifested in small band gap areas. By summing up the AHC values obtained from only the blue areas, we obtain a total AHC of around -592.2 S cm^{-1} . Therefore, the peak value of AHC around the Fermi level can be well reproduced by considering only the blue areas in the BZ, whereas the other areas have limited contribution to the total AHC (see Figure 5b).

We then select a specific k path on this k plane, that is, from k_1 to k_2 which are marked out by the cross symbols, to

investigate how the band structure changes by including the SOC effect. It can be clearly seen from Figure 5d that the band crossings between the spin-up and spin-down channels in the spin-polarized calculation without SOC effect are avoided when SOC effect is considered, resulting in the continuous small band gap opening slightly below the Fermi level along the selected k path. Therefore, the singular AHC and ANC in Ni_2VMn are mainly driven by a gap opening of nodal lines due to SOC.

Based on the current HTP work, it is also interesting to inspect the correlations between the transport properties, that is, AHC, AHC_{max} , ANC, ANC_{max} , and the number of valence electrons (N_v). We inspect such correlations separately in cubic and tetragonal Heuslers, as displayed in Figure 6a–d. We find that for regular cubic Heuslers, the peak for both AHC and ANC usually occurs for $N_v \in [26, 28]$, whereas the summits are usually seen for $N_v > 30$, particularly for $N_v \in [36, 40]$, in tetragonal Heuslers. Such correlations can be understood from the point that the number of valence electrons is related to the band filling of the band structure. Namely, certain valence electron counting can move the Fermi level closer to the topological features, thus leading to higher AHC and ANC. Clearly, the band filling behaves differently in cubic and tetragonal structures. However, it should be reminded that large AHC does not necessarily means large ANC, as pointed out in Ref. [28]. We also notice that, despite the different space groups the cubic and tetragonal Heuslers belong to, they actually have the same magnetic Laue group $4/\text{mm}'\text{m}'$ under the studied ferro/ferri-magnetic state. From a symmetry

Table 2. Symmetry operations of the magnetic Laue group $4/m\bar{m}'m'$ and the relation with chirality. Here (x, y, z) form includes the time reversal symmetry.

N	(x, y, z) form	TR	Seitz Symbol	Chirality
1	x, y, z	1	1	1
2	$-x, -y, z$	1	2_z	1
3	$-y, x, z$	1	4_z	1
4	$y, -x, z$	1	4_z^{-1}	1
5	$-x, -y, -z$	1	-1	-1
6	$x, y, -z$	1	m_z	-1
7	$y, -x, -z$	1	-4_z	-1
8	$-y, x, -z$	1	-4_z^{-1}	-1
9	$-x, y, z$	-1	$2'_x$	1
10	$x, -y, z$	-1	$2'_y$	1
11	y, x, z	-1	$2'_{-xy}$	1
12	$-y, -x, z$	-1	$2'_{xy}$	1
13	$x, -y, -z$	-1	m'_x	-1
14	$-x, y, -z$	-1	m'_y	-1
15	$-y, -x, -z$	-1	m'_{-xy}	-1
16	$y, x, -z$	-1	m'_{xy}	-1

point view, their belonging to the same magnetic Laue group renders the similarity in their performances on the transport properties. By classifying the absolute values of AHC/ANC by the space group, we indeed find that the maxima, as well as the averages of the AHC/ANC for space group no. 139 and no. 225 are almost equivalent. The maximum and average of AHC in both cubic and tetragonal Heuslers are around 2000 and 370 $S\text{ cm}^{-1}$, respectively. Similarly, the maximum and average of ANC at 300 K in both cubic and tetragonal Heuslers are about 10.0 and 1.8 $\text{A m}^{-1}\text{K}^{-1}$, respectively.

3. Conclusion

In summary, we have carried out a HTP screening of all- d regular magnetic Heuslers, including both cubic and tetragonal

compounds, to search for Heuslers with large AHC/ANC. A giant AHC of 2011 $S\text{ cm}^{-1}$ at the Fermi level has been found in cubic Re_2TaMn , following the tetragonal Pt_2RhCr with an AHC of 1966 $S\text{ cm}^{-1}$. Interestingly, Co_2NbMn and Fe_2NiCo , which consist of more abundant elements, are predicted to have rather high |AHC| at the Fermi level, being approximately 1210 and 1043 $S\text{ cm}^{-1}$, respectively. Additionally, Os_2TaCr and Pt_2RhCo exhibit high magnitudes of |ANC| being 9.7 and 9.5 $\text{A m}^{-1}\text{K}^{-1}$, respectively, which are comparable to the highest ANC reported hitherto of $\text{Co}_3\text{Sn}_2\text{S}$. The current work also reveals the determining role of symmetry on the topological properties. Belonging to the same magnetic Laue group $4/m\bar{m}'m'$, the ferro/ferri-magnetic cubic and tetragonal Heuslers display similar performance regarding the maxima and averages of |AHC|/|ANC|. Moreover, we find that the AHC/ANC values are mainly contributed by the Weyl points, avoided band crossings, as well as the nodal lines with small band gaps.

Furthermore, the exact position of the BC with respect to the Fermi level significantly influences the transport properties. Therefore, we illustrate separately for cubic and tetragonal Heuslers the correlations between the AHC, AHC, AHC_{max} , ANC, ANC_{max} and the number of valence electrons N_v . For cubic Heuslers, we have identified $N_v \in [26, 28]$ as the sweet points, whereas for tetragonal Heuslers, the compounds with $N_v \in [36, 40]$ stand out. Such statistical analysis provides a valuable guidance for tailoring the transport properties of Heuslers via altering the band filling by, for example, chemical doping, as recently reported for $\text{Fe}_3\text{Sn}^{[53]}$ and $(\text{Ti,Zr,Hf})\text{MnP}^{[54]}$

4. Experimental Section

A total of 344 Heusler compounds X_2YZ , which have negative formation energies and convex hull distance smaller than 175 meV per atom, were selected for the evaluation of the topological transport properties (AHC and ANC) based on our HTP calculations.^[38] For Heuslers X_2YZ , X (0.25, 0.25, 0.25), Y (0.00, 0.00, 0.00), and Z (0.50, 0.50, 0.50) are one of the $3d/4d/5d$ elements except Tc, and at least one magnetic $3d$ element (V, Cr, Mn, Fe, Co, Ni) is on either the X or the Y/Z sites. The selected materials were thermodynamically stable/metastable, FM or ferrimagnetic in nature, and had regular cubic or regular tetragonal ground state structure. The calculations were automated by using an in-house developed workflow^[55,56] that integrates VASP,^[57-59] Wannier90,^[60]

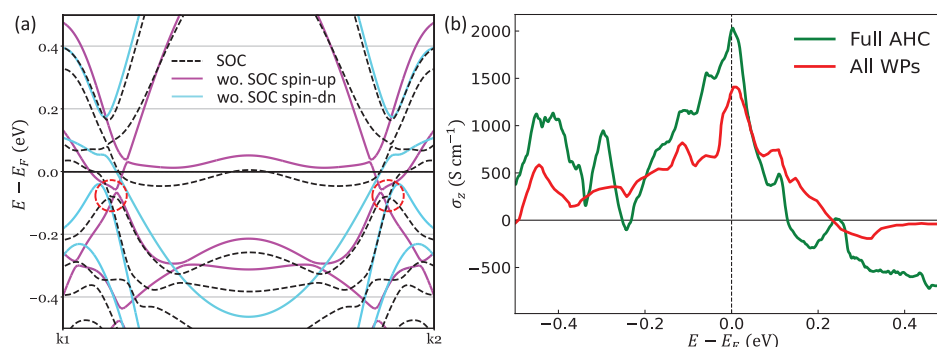


Figure 3. a) The band structure of primitive Re_2TaMn along the k path from k_1 (-0.10, 0.35, 0.41) to k_2 (0.35, -0.10, 0.41) which crosses a pair of Weyl nodes (marked out by red dashed circles) with spin-orbit coupling (SOC) effect included. The band structure in the spin-polarized case without SOC is shown for comparison b) The z -component of the AHC (σ_z) (green) and the contribution from all Weyl points to AHC (red) as a function of energy (with respect to the Fermi level) for Re_2TaMn with magnetization along the [001] direction.

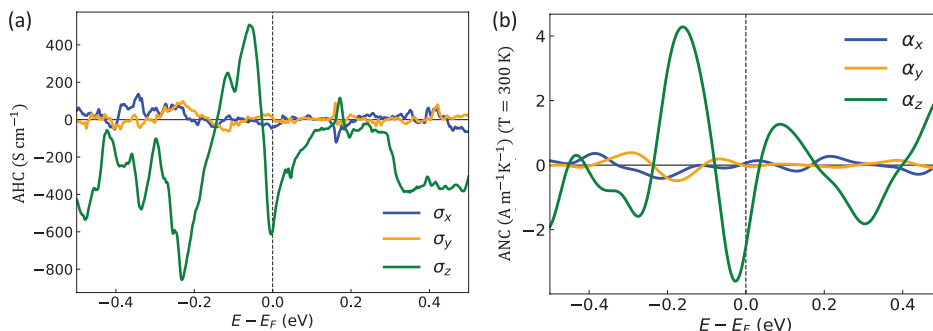


Figure 4. a) The components of the calculated AHC, σ_x , σ_y , and σ_z , and b) the calculated ANC at 300 K, α_x , α_y , and α_z , of Ni₂VMn for the magnetization direction along the [001] direction with respect to the Fermi energy.

and WannierTools^[61] software packages. First, the DFT calculations were conducted using VASP, in which the projected augmented wave (PAW)^[62,63] method and the exchange-correlation functional of GGA-PBE^[64] were implemented. All the calculations included the SOC effect. The k mesh used for the calculations, being Γ -centred, had a density of 50 with respect to the lattice parameter. The cut-off energy for the plane waves was set to 500 eV. Subsequently, the maximally localized Wannier functions (MLWFs)^[65] were constructed using the Wannier90 code. The required parameters, such as the number of projection orbitals and the disentanglement and frozen windows, were chosen automatically according to the algorithm proposed by Zhang *et al.*^[55] Lastly, the intrinsic AHC was evaluated using WannierTools based on

the tight binding model constructed from the MLWFs, which is defined as the integration of BC over the entire BZ. Summing over all of the occupied bands, the AHC can be obtained according to the following formula^[66]

$$\sigma_{\alpha\beta} = -\frac{e^2}{h} \int \frac{dk}{(2\pi)^3} \sum_n f[\varepsilon(k) - \mu] \Omega_{n,\alpha\beta}(k), \quad (3)$$

with BC itself calculated according to

$$\Omega_{n,\alpha\beta}(k) = -2\text{Im} \sum_{m \neq n} \frac{\langle kn | v_\alpha(k) | km \rangle \langle km | v_\beta(k) | kn \rangle}{[\varepsilon_m(k) - \varepsilon_n(k)]^2}, \quad (4)$$

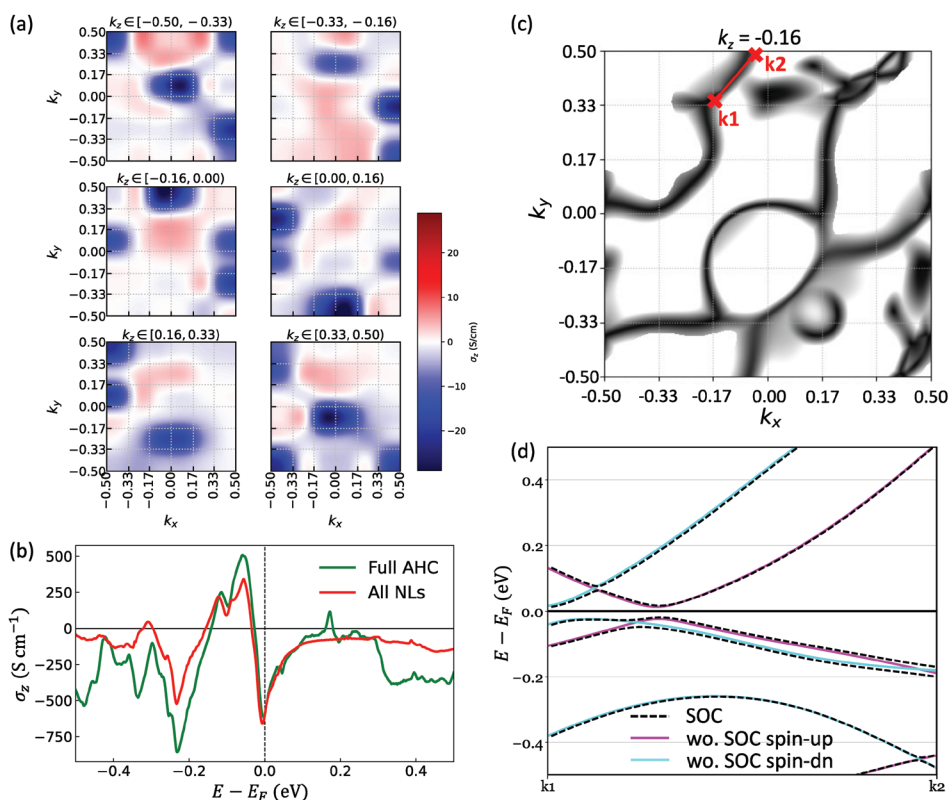


Figure 5. a) The z-component of the AHC evaluated in 216 Brillouin Zone cubes for Ni₂VMn with magnetization direction parallel to the [001] axis. b) The z-component of the AHC (σ_z) (green) and the contribution from the nodal lines (NLs) to AHC (red) as a function of energy for Ni₂VMn with magnetization along the [001] direction. c) Small band gap area between bands in the vicinity of Fermi level at a slice of Brillouin zone of $k_z = -0.16$. d) The calculated band structure with spin-orbit coupling (SOC) effect along the path from k_1 to k_2 is compared with that of spin-polarized calculation without SOC effect.

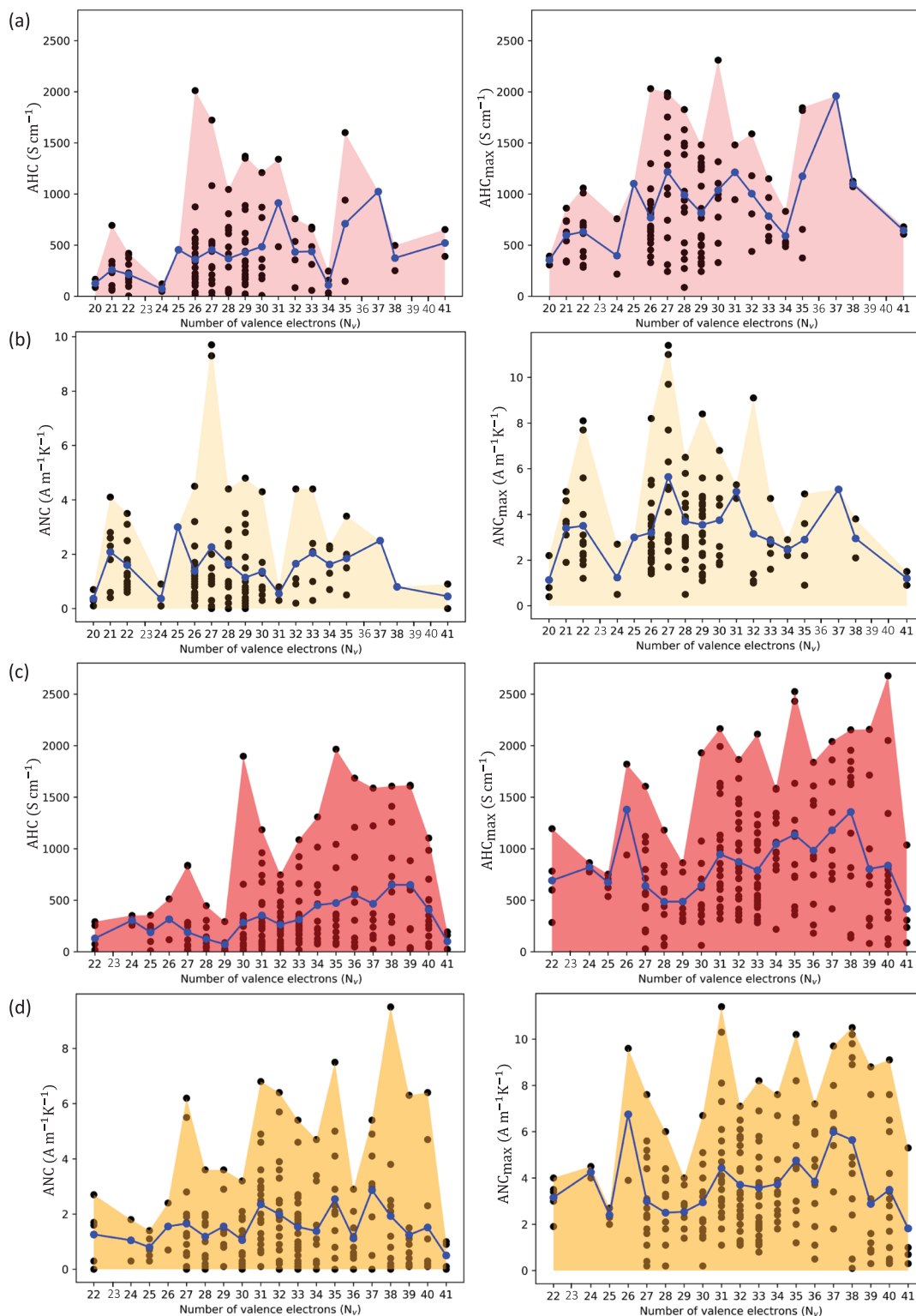


Figure 6. a) The AHC at Fermi level, AHC_{max} , b) ANC at Fermi level, ANC_{max} at 300 K with respect to the number of valence electrons (N_v) for regular cubic all- d Heuslers; c) the AHC at Fermi level, AHC_{max} , d) ANC at Fermi level, ANC_{max} at 300 K with respect to the number of valence electrons (N_v) for regular tetragonal all- d Heuslers.

in which μ stands for the Fermi energy, n and m for the occupied and unoccupied bands, respectively, and $\varepsilon_n(\mathbf{k})$ and $\varepsilon_m(\mathbf{k})$ for the

corresponding eigenvalues. $f[\varepsilon(\mathbf{k}) - \mu]$ represents the Fermi distribution function. The v_α and v_β are velocity operators. In order to evaluate the

AHC, a k mesh having the density of 400 with respect to the lattice parameter was used to guarantee good convergence. The ANC was calculated by evaluating the following integral,^[67]

$$\alpha_{\alpha\beta} = -\frac{1}{e} \int d\varepsilon \frac{\partial f}{\partial \mu} \sigma_{\alpha\beta}(\varepsilon) \frac{\varepsilon - \mu}{T}, \quad (5)$$

where ε represents the energy of a point in the energy grid, e and T are respectively the electron charge and the temperature. The above integral was evaluated using an energy grid containing 1001 points within the range [-0.5, 0.5] eV with respect to the Fermi level at 300 K. The detailed analysis on the origin of AHC utilized the available features of WannierTools,^[68,69] including the search for Weyl or nodal points, and the calculations of chirality, BC, *etc.*

Supporting Information

Supporting Information is available from the Wiley Online Library or from the author.

Acknowledgements

M.F.T. and N.F. contributed equally to this work. The Lichtenberg high performance computer of the TU Darmstadt was gratefully acknowledged for the computational resources where the calculations were conducted for this project. This project was supported by the Deutsche Forschungsgemeinschaft (DFG, German Research Foundation)-Project-ID 40553726-TRR 270, and the European Research Council (ERC) under the European Union's Horizon 2020 research and innovation programme (grant no. 743116-project Cool Innov)

Open access funding enabled and organized by Projekt DEAL.

Conflict of Interest

The authors declare no conflict of interest.

Data Availability Statement

The data that support the findings of this study are available from the corresponding author upon reasonable request.

Keywords

all-d heusler, high-throughput, transport properties

Received: December 23, 2022

Revised: March 9, 2023

Published online: April 23, 2023

[1] D. Xiao, M.-C. Chang, Q. Niu, *Rev. Mod. Phys.* **2010**, *82*, 1959.

[2] B. Yan, S.-C. Zhang, *Rep. Prog. Phys.* **2012**, *75*, 096501.

[3] B. Yan, C. Felser, *Annu. Rev. Condens. Matter Phys.* **2017**, *8*, 337.

[4] N. Armitage, E. Mele, A. Vishwanath, *Rev. Mod. Phys.* **2018**, *90*, 015001.

[5] Q. L. He, T. L. Hughes, N. P. Armitage, Y. Tokura, K. L. Wang, *Nat. Mater.* **2022**, *21*, 15.

[6] L. Šmejkal, Y. Mokrousov, B. Yan, A. H. MacDonald, *Nat. Phys.* **2018**, *14*, 242.

[7] E. M. Pugh, N. Rostoker, *Rev. Mod. Phys.* **1953**, *25*, 151.

[8] N. Nagaosa, J. Sinova, S. Onoda, A. H. MacDonald, N. P. Ong, *Rev. Mod. Phys.* **2010**, *82*, 1539.

[9] A. Gerber, A. Milner, M. Karpovsky, B. Lemke, H.-U. Habermeier, J. Tuailon-Combes, M. Négrier, O. Boisson, P. Mélinon, A. Perez, *J. Magn. Magn. Mater.* **2002**, *242*, 90.

[10] Y. Sakuraba, *Scr. Mater.* **2016**, *111*, 29.

[11] W. Zhou, Y. Sakuraba, *Appl. Phys. Express* **2020**, *13*, 043001.

[12] K. I. Uchida, J. P. Heremans, *Joule* **2022**, *6*, 2240.

[13] T. Graf, C. Felser, S. S. Parkin, *Prog. Solid State Chem.* **2011**, *39*, 1.

[14] J. Hu, S. Granville, H. Yu, *Ann. Phys.* **2020**, *532*, 1900456.

[15] S. Chadov, X. Qi, J. Kübler, G. H. Fecher, C. Felser, S. C. Zhang, *Nat. Mater.* **2010**, *9*, 541.

[16] K. Manna, L. Muechler, T.-H. Kao, R. Stinshoff, Y. Zhang, J. Gooth, N. Kumar, G. Kreiner, K. Koepfner, R. Car, J. Kübler, G. H. Fecher, C. Shekhar, Y. Sun, C. Felser, *Phys. Rev. X* **2018**, *8*, 041045.

[17] S. Ouardi, G. H. Fecher, C. Felser, J. Kübler, *Phys. Rev. Lett.* **2013**, *110*, 100401.

[18] Q. Gao, I. Opahle, H. Zhang, *Phys. Rev. Mater.* **2019**, *3*, 024410.

[19] K. Manna, Y. Sun, L. Muechler, J. Kübler, C. Felser, *Nat. Rev. Mater.* **2018**, *3*, 244.

[20] H. Reichlova, R. Schlitz, S. Beckert, P. Swekis, A. Markou, Y.-C. Chen, D. Kriegner, S. Fabretti, G. Hyeon Park, A. Niemann, S. Sudheendra, A. Thomas, K. Nielsch, C. Felser, S. T. B. Goennenwein, *Appl. Phys. Lett.* **2018**, *113*, 212405.

[21] A. Sakai, Y. P. Mizuta, A. A. Nugroho, R. Sihombing, T. Koretsune, M.-T. Suzuki, N. Takemori, R. Ishii, D. Nishio-Hamane, R. Arita, P. Goswami, S. Nakatsuji, *Nat. Phys.* **2018**, *14*, 1119.

[22] I. Belopolski, K. Manna, D. S. Sanchez, G. Chang, B. Ernst, J. Yin, S. S. Zhang, T. Cochran, N. Shumiya, H. Zheng, B. Singh, G. Bian, D. Multer, M. Litskevich, X. Zhou, S.-M. Huang, B. Wang, T.-R. Chang, S.-Y. Xu, A. Bansil, C. Felser, H. Lin, M. Z. Hasan, *Science* **2019**, *365*, 1278.

[23] S. N. Guin, K. Manna, J. Noky, S. J. Watzman, C. Fu, N. Kumar, W. Schnelle, C. Shekhar, Y. Sun, J. Gooth, C. Felser, *NPG Asia Mater.* **2019**, *11*, 16.

[24] Y. Sakuraba, K. Hyodo, A. Sakuma, S. Mitani, *Phys. Rev. B* **2020**, *101*, 134407.

[25] W. Zhou, K. Yamamoto, A. Miura, R. Iguchi, Y. Miura, K.-I. Uchida, Y. Sakuraba, *Nat. Mater.* **2021**, *20*, 463.

[26] H. Zhang, *Electron. Struct.* **2021**, *3*, 033001.

[27] I. Samathrakris, T. Long, Z. Zhang, H. K. Singh, H. Zhang, *J. Phys. D: Appl. Phys.* **2021**, *55*, 074003.

[28] J. Noky, Y. Zhang, J. Gooth, C. Felser, Y. Sun, *npj Comput. Mater.* **2020**, *6*, 77.

[29] Y. Ji, W. Zhang, H. Zhang, W. Zhang, *New J. Phys.* **2022**, *24*, 053027.

[30] Z. Wei, E. Liu, J. Chen, Y. Li, G. Liu, H. Luo, X. Xi, H. Zhang, W. Wang, G. Wu, *Appl. Phys. Lett.* **2015**, *107*, 022406.

[31] A. Taubel, B. Beckmann, L. Pfeuffer, N. Fortunato, F. Scheibel, S. Ener, T. Gottschall, K. P. Skokov, H. Zhang, O. Gutfleisch, *Acta Mater.* **2020**, *201*, 425.

[32] A. Aznar, A. Gràcia-Condal, A. Planes, P. Lloveras, M. Barrio, J.-L. Tamarit, W. Xiong, D. Cong, C. Popescu, L. Mañosa, *Phys. Rev. Mater.* **2019**, *3*, 044406.

[33] Y. Han, A. Bouhemadou, R. Khenata, Z. Cheng, T. Yang, X. Wang, *J. Magn. Magn. Mater.* **2019**, *471*, 49.

[34] Y. Han, M. Wu, Y. Feng, Z. Cheng, T. Lin, T. Yang, R. Khenata, X. Wang, *IUCrj* **2019**, *6*, 465.

[35] V. G. de Paula, M. S. Reis, *Chem. Mater.* **2021**, *33*, 5483.

[36] K. Özdoğan, I. V. Maznichenko, S. Ostanin, E. Şaşıoğlu, A. Ernst, I. Mertig, I. Galanakis, *J. Phys. D: Appl. Phys.* **2019**, *52*, 205003.

[37] S. Sanvito, C. Oses, J. Xue, A. Tiwari, M. Zic, T. Archer, P. Tozcan, M. Venkatesan, M. Coey, S. Curtarolo, *Sci. Adv.* **2017**, *3*, e1602241.

[38] N. Fortunato, I. Ophale, L. Pfeuffer, A. Taubel, F. Scheibel, O. Gutfleisch, H. Zhang. HTP design of all- d -metal Heuslers for energy applications.

- [39] L. Šmejkal, R. González-Hernández, T. Jungwirth, J. Sinova, *Sci. Adv.* **2020**, *6*, eaaz8809.
- [40] M. Yu, G. Li, C. Fu, E. Liu, K. Manna, E. Budiyanto, Q. Yang, C. Felser, H. Tüysüz, *Angew. Chem., Int. Ed.* **2021**, *60*, 5800.
- [41] F. Garmroudi, M. Parzer, M. Knopf, A. Riss, H. Michor, A. Ruban, T. Mori, E. Bauer, *Phys. Rev. B* **2023**, *107*, 014108.
- [42] S. N. Guin, K. Manna, J. Noky, S. J. Watzman, C. Fu, N. Kumar, W. Schnelle, C. Shekhar, Y. Sun, J. Gooth, C. Felser, *NPG Asia Mater.* **2019**, *11*, 16.
- [43] J.-C. Tung, G.-Y. Guo, *New J. Phys.* **2013**, *15*, 033014.
- [44] M. Singh, H. S. Saini, J. Thakur, A. H. Reshak, M. K. Kashyap, *J. Magn. Magn. Mater.* **2014**, *370*, 81.
- [45] H. Yang, W. You, J. Wang, J. Huang, C. Xi, X. Xu, C. Cao, M. Tian, Z.-A. Xu, J. Dai, Y. Li, *Phys. Rev. Mater.* **2020**, *4*, 024202.
- [46] W. Zhou, T. Hirai, K.-I. Uchida, Y. Sakuraba, *J. Phys. D: Appl. Phys.* **2022**, *55*, 335002.
- [47] H. Zhang, S. Blügel, Y. Mokrousov, *Phys. Rev. B* **2011**, *84*, 024401.
- [48] M.-T. Suzuki, T. Koretsune, M. Ochi, R. Arita, *Phys. Rev. B* **2017**, *95*, 094406.
- [49] M. V. Berry, *Proc. R. Soc. London* **1984**, *392*, 45.
- [50] D. Vanderbilt, *Berry phases in electronic structure theory: Electric polarization, orbital magnetization and topological insulators*, Cambridge University Press, Cambridge, **2018**.
- [51] H. K. Singh, I. Samathrakris, N. M. Fortunato, J. Zemen, C. Shen, O. Gutfleisch, H. Zhang, *npj Comput. Mater.* **2021**, *7*, 98.
- [52] H. B. Nielsen, M. Ninomiya, *Nucl. Phys. B* **1981**, *185*, 20.
- [53] C. Shen, I. Samathrakris, K. Hu, H. K. Singh, N. Fortunato, H. Liu, O. Gutfleisch, H. Zhang, *npj Comput. Mater.* **2022**, *8*, 248.
- [54] I. Samathrakris, N. Fortunato, H. K. Singh, C. Shen, H. Zhang, *J. Phys.: Condens. Matter* **2022**, *51*, 025703.
- [55] Z. Zhang, R.-W. Zhang, X. Li, K. Koepf, Y. Yao, H. Zhang, *J. Phys. Chem. Lett.* **2018**, *9*, 6224.
- [56] Automatic-wannier-flow, <https://github.com/TMM-TUDA/Automatic-wannier-flow>.
- [57] G. Kresse, J. Hafner, *Phys. Rev. B* **1993**, *47*, 558.
- [58] G. Kresse, J. Hafner, *Phys. Rev. B* **1994**, *49*, 14251.
- [59] G. Kresse, J. Furthmüller, *Comput. Mater. Sci.* **1996**, *6*, 15.
- [60] A. A. Mostofi, J. R. Yates, G. Pizzi, Y.-S. Lee, I. Souza, D. Vanderbilt, N. Marzari, *Comput. Phys. Commun.* **2014**, *185*, 2309.
- [61] Q. Wu, S. Zhang, H.-F. Song, M. Troyer, A. A. Soluyanov, *Comput. Phys. Commun.* **2018**, *224*, 405.
- [62] P. E. Blöchl, *Phys. Rev. B* **1994**, *50*, 17953.
- [63] G. Kresse, D. Joubert, *Phys. Rev. B* **1999**, *59*, 1758.
- [64] J. P. Perdew, K. Burke, M. Ernzerhof, *Phys. Rev. Lett.* **1996**, *77*, 3865.
- [65] N. Marzari, A. A. Mostofi, J. R. Yates, I. Souza, D. Vanderbilt, *Rev. Mod. Phys.* **2012**, *84*, 1419.
- [66] X. Wang, J. R. Yates, I. Souza, D. Vanderbilt, *Phys. Rev. B* **2006**, *74*, 195118.
- [67] D. Xiao, Y. Yao, Z. Fang, Q. Niu, *Phys. Rev. Lett.* **2006**, *97*, 026603.
- [68] R. Yu, X. L. Qi, A. Bernevig, Z. Fang, X. Dai, *Phys. Rev. B* **2011**, *84*, 075119.
- [69] A. A. Soluyanov, D. Vanderbilt, *Phys. Rev. B* **2011**, *83*, 035108.